ACS APPLIED BIO MATERIALS

www.acsabm.org Article

# Engineering of $CoSe_2$ Nanosheets via Vacancy Manipulation for Efficient Cancer Therapy

Mingyang Liu, Qilin Yu,* Wei Chen, Xiangsheng Liu,* and Pedro J. J. Alvarez*

Cite This: *ACS Appl. Bio Mater.* 2020, 3, 7800–7809 Read Online

ACCESS | Metrics & More | Article Recommendations | Supporting Information

**ABSTRACT:** $CoSe_2$ nanosheets with different vacancy associates (*i.e.*, $V_{SeSe}$, $V_{CoCoSe}$, $V_{CoSeSe}$, and $V_{CoCoCoSe}$) were synthesized by selecting different templates and calcination temperatures. The nanosheets having higher theoretical adsorption toward cellular membrane phospholipids exerted more damage to both artificial liposomes and cell membranes ($V_{SeSe} > V_{CoCoSe} > V_{CoCoCoSe} > V_{CoSeSe}$) and exhibited higher efficiency to kill tumor cells (*e.g.*, A549 lung cancer cells and HeLa cervical cancer cells). Moreover, $V_{CoCoCoSe}$ $CoSe_2$ nanosheets can be easily coated with the tumor-targeting protein transferrin (Tf), and these Tf-coated nanosheets (Tf-$V_{CoCoCoSe}$) drastically decreased the viability of various types of cancer cells (81%) without significantly damaging normal cells. Importantly, this treatment was more efficient in eliminating tumor tissues than the common chemotherapeutic drug oxaliplatin. Thus, this study offers proof of concept that manipulating the surface vacancies of $CoSe_2$ nanosheets could provide an efficient route for cancer therapy in a manner that could circumvent or minimize drug resistance development.

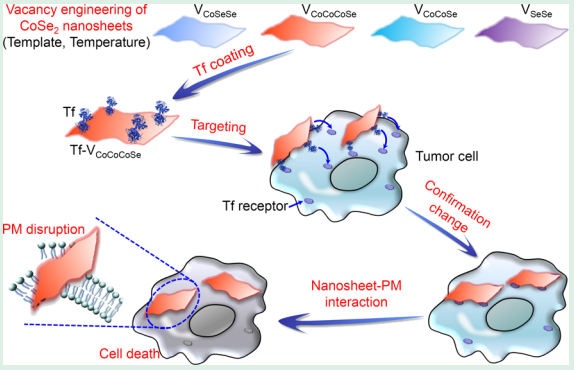


**KEYWORDS:** *vacancy engineering, $CoSe_2$ nanosheet, transferrin, plasma membrane, cancer therapy*

## 1. INTRODUCTION

Chemotherapy is one of the most important strategies to treat cancer.[1−3] However, its efficiency is compromised by the limited selectivity of common chemotherapeutic drugs (*e.g.*, oxaliplatin, camptothecin, doxorubicin, cisplatin, and paclitaxel), which results in collateral damage of healthy cells and development of drug resistance.[4−6] Nanotechnology-based chemotherapy that uses tumor-targeting, ligand-modified nanocarriers for drug delivery, *e.g.*, liposomes and polymeric nanoparticles coated with transferrin to target transferrin receptors, which are abundant on tumor cell surfaces, can enhance the selectivity of chemotherapeutic drugs and minimize collateral damage.[7−10] However, nanocarrier-mediated cancer therapies only partially evade the development of drug resistance due to various intracellular processes (*e.g.*, drug inactivation, alteration of drug targets, activation of adaptive responses, loss of cell death induction, poor drug influx, and excessive efflux).[11−14] This underscores the need for alternative therapeutic strategies that circumvent or minimize drug resistance development. For example, anticancer drugs could be replaced or supplemented with nanomaterials (NMs) that directly target the plasma membrane (PM) of tumor cells, whose damage can lead to rapid tumor cell death.[15,16] Accordingly, NMs' structures and properties could be manipulated to enhance cell killing reactivity, and selective killing of tumor cells could be further enhanced by surface modification with targeting ligands.[17−19]

Among many emerging NMs used for nanomedicine, two-dimensional (2D) NMs such as GO, $MoS_2$, $MoSe_2$, Ti, and Xenes hold great promise for various applications due to their unique physiochemical properties and biological activity.[20−23] Particularly, these NMs may interact with the membrane components and alter the membrane structure and permeability.[24,25] Many studies have shown a link between the surface defect/vacancy and physiochemical characteristics of NMs, including their magnetic, optical, electronic properties.[26−30] This suggests that vacancy manipulation might be a viable (yet overlooked) approach to control the reactivity of crystalline NMs and enhance their ability to kill tumor cells. Supporting circumstantial evidence includes a report that increasing the abundance of vacancies on $Bi_2S_3$−Au heterojunction nanorods for photothermal therapy significantly enhanced the efficacy of cancer treatment.[31]

Received: August 6, 2020
Accepted: October 15, 2020
Published: October 30, 2020

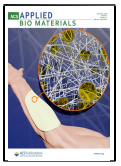






https://dx.doi.org/10.1021/acsabm.0c00981
*ACS Appl. Bio Mater.* 2020, 3, 7800–7809

$CoSe_2$ nanosheets are emerging 2D NMs that are used for electrocatalysis, energy storage, and hydrogen evolution.[32−34] Their vacancies could be easily regulated for improving their surface characteristics.[20,21] Owing to the convenience of surface vacancy manipulation for regulation of surface activity when interacting with biological systems, it is anticipated that $CoSe_2$ nanosheets may be developed as novel 2D NMs for biomedical applications.

Herein, we present a new facile strategy for efficient antitumor therapy through vacancy engineering of $CoSe_2$ nanosheets by easily controlling templates (triethylene tetramine (TETA) or tetraethylenepentamine (TEPA)) and calcination temperatures, obtaining the nanosheets with the vacancies of $V_{CoSeSe}$ (TETA, 200 °C), $V_{CoCoCoSe}$ (TETA, 250 °C), $V_{CoCoSe}$ (TEPA, 260 °C), and $V_{SeSe}$ (TEPA, 225 °C) (Figure 1). Theoretical calculations, phospholipid adsorption,

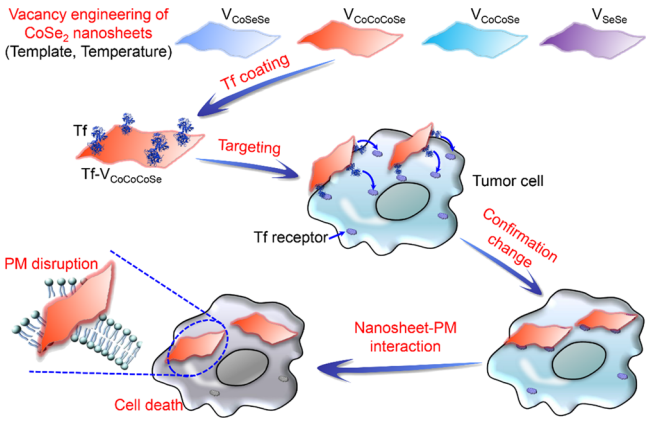


**Figure 1.** Schematic illustration of vacancy engineering and transferrin coating of $CoSe_2$ nanosheets to facilitate targeting cancer therapy.

and cell viability assays revealed that the nanosheets had vacancy-dependent interaction with the membrane phospholipids and damage to tumor cells. The $V_{CoCoCoSe}$ nanosheets (which were easier to coat with the tumor-targeting protein transferrin (Tf) than nanosheets with other vacancies) could specifically target and kill the tumor cells, exhibiting strong anticancer activity both *in vitro* and *in vivo*. Overall, our experimental results supported by first-principles computations and benchmarking against the common chemotherapeutic drug oxaliplatin suggest that manipulating vacancies on the surface of crystalline NMs may lead to a simple, convenient, and efficient approach for cancer therapy.

## 2. EXPERIMENTAL SECTION

**2.1. Synthesis of $CoSe_2$ Nanosheets.** $CoCl_2$ (1.0 g) was added into a 50 mL beaker, and then 15 mL of TETA (or TEPA) and 15 mL of ethylene glycol were added with magnetic stirring for 0.5 h to form a homogeneous solution. Next, 0.4371 g of Se powder was added, and then 10 mL of ethylene diamine was added. Subsequently, the mixture was transferred into a Teflon-lined stainless steel autoclave with a capacity of 50 mL for solvothermal treatment at 150 °C for 20 h. After the autoclave was cooled to room temperature, the precipitate was separated by centrifugation, washed with water and absolute ethanol to remove impurities, and then dried at 80 °C, resulting in the precursor of $CoSe_2$ nanosheets.

**2.2. Characterization.** The phase of the samples was characterized by XRD under a Rigaku D/Max (EAST) Ultima II Powder XRD 6s X-ray diffractometer, employing Cu K$\alpha$ radiation, $\lambda$ = 1.54056 Å. The morphology and size of the samples were characterized using a field emission scanning electron microscope (FEI Quanta 400 ESEM FEG) and HRTEM (JEOL 2100 field emission gun transmission electron microscope).

**2.3. Positron Annihilation Measurement.** The positron lifetime experiments were conducted using a fast-slow coincidence ORTEC system with a time resolution of ∼230 ps full width at half-maximum. A 5 mCi source of $^{22}Na$ was sandwiched between two identical samples, with a total count of 1 million. Positron lifetime calculations were performed using the atomic superposition method[35−37] in which the electron density and the positron crystalline Coulombic potential were constructed by the non-self-consistent superposition of free atom electron density and Coulombic potential in the absence of the positron. The calculations of the positron lifetime were performed using the electron-positron enhancement factor according to Barbiellini's generalized gradient approximation.[38] Positron lifetime calculations were performed for unrelaxed structure monovacancy defects and vacancy associates in $CoSe_2$ using 3 × 3 × 2 supercells.

**2.4. First-Principles Computation.** To corroborate our hypothesis, we computed the adsorption energy of the $V_{CoCoCoSe}$ vacancies nanosheets for liposomes using the simple molecule $CH_3NH_2$, which similarly to phospholipids has both $-CH_3$ and $-NH_2$ groups, to represent liposomes.[39] Our first-principles computations were performed using the projector augmented wave (PAW) approach to represent the ion−electron interaction,[40] as implemented in the Vienna *ab initio* simulation package.[41] The electron exchange−correlation functional was treated using generalized gradient approximation in the form proposed by Perdew, Burke, and Ernzerhof.[42] The energy and force precision were set to $10^{-4}$ eV and $10^{-2}$ eV/Å, respectively. The energy cutoff was set as 580 eV and the Brillouin zone was sampled with a 3 × 3 × 1 Γ-centered Monkhorst-Pack *k*-point grid for geometry optimization of slabs models.

The $CoSe_2$ slab along the [101] direction was cleaved from the bulk $CoSe_2$ crystal, which both belong to the orthorhombic space group *Pnnm* (no. 58), as shown in Figure S4. The slab models have the thickness of five atomic layers for the simulation of the as-prepared $CoSe_2$ samples with the (101) facet. The slabs were placed in the *xy* plane with the *z* direction perpendicular to the layer plane and a vacuum space of 20 Å in the *z* direction was used to avoid interactions between adjacent layers and adsorbed molecules. Additionally, the vacancies of $V_{SeSe}$, $V_{CoSeSe}$, $V_{CoCoSe}$, and $V_{CoCoCoSe}$ on the (101) surface of $CoSe_2$ were simulated by removing two Se atoms, one Co and two Se atoms, and two Co and one Se atoms (or three Co and one Se atoms) from the slab model, respectively.

The adsorption properties of $CoSe_2$ (101) facets with $V_{SeSe}$, $V_{CoSeSe}$, $V_{CoCoSe}$, and $V_{CoCoCoSe}$ vacancies were theoretically analyzed by computing the adsorption energies of the $CH_3NH_2$ molecule on the (101) surface of $CoSe_2$ with corresponding facets. The adsorption energy was defined as the following equation: $E_{ad} = E_{total\text{-}vacancy} - E_{slab\text{-}vacancy} - E_{molecule})/S$. In this equation, $E_{total}$, $E_{slab}$, and $E_{molecule}$ are the energy of the adsorption system in total, the slab system with cluster adsorption, and the $CH_3NH_2$ molecule, respectively,[43] while *S* presents the surface area of the $CoSe_2$ (101) facet.

**2.5. Cell Culture.** All of the used cells were obtained from the Cell Resource Center, Chinese Academy of Medical Science, Beijing, China. The human cervical cancer cells (HeLa), the mouse fibroblast (NIH3T3), and the human embryonic lung fibroblasts (MRC-5) were cultured in Dulbecco's modified Eagle's medium (DMEM) supplemented with 10% fetal bovine serum (FBS). The human lung cancer cells (A549) were cultured in F-12 medium supplemented with 10% FBS. The cells were incubated in 24-well flat-bottom polystyrene plates within a humidified incubator at 37 °C in 5% $CO_2$ for 24 h for further experiments.

**2.6. Cell Viability and Apoptosis Assays.** The cells were treated by uncoated or coated $CoSe_2$ nanosheets (0−80 mg/L or 20 mg/L for most experiments) for 24 h. Cell viability and apoptosis of the treated cells were assessed using a CCK-8 cell viability kit (Beyotime, China) and an FITC-Annexin V kit (Sungene Biotech, China), respectively. The fluorescence density of the stained cells was analyzed using a flow cytometer (FACSCalibur, Becton Dickinson,


https://dx.doi.org/10.1021/acsabm.0c00981
ACS Appl. Bio Mater. 2020, 3, 7800−7809

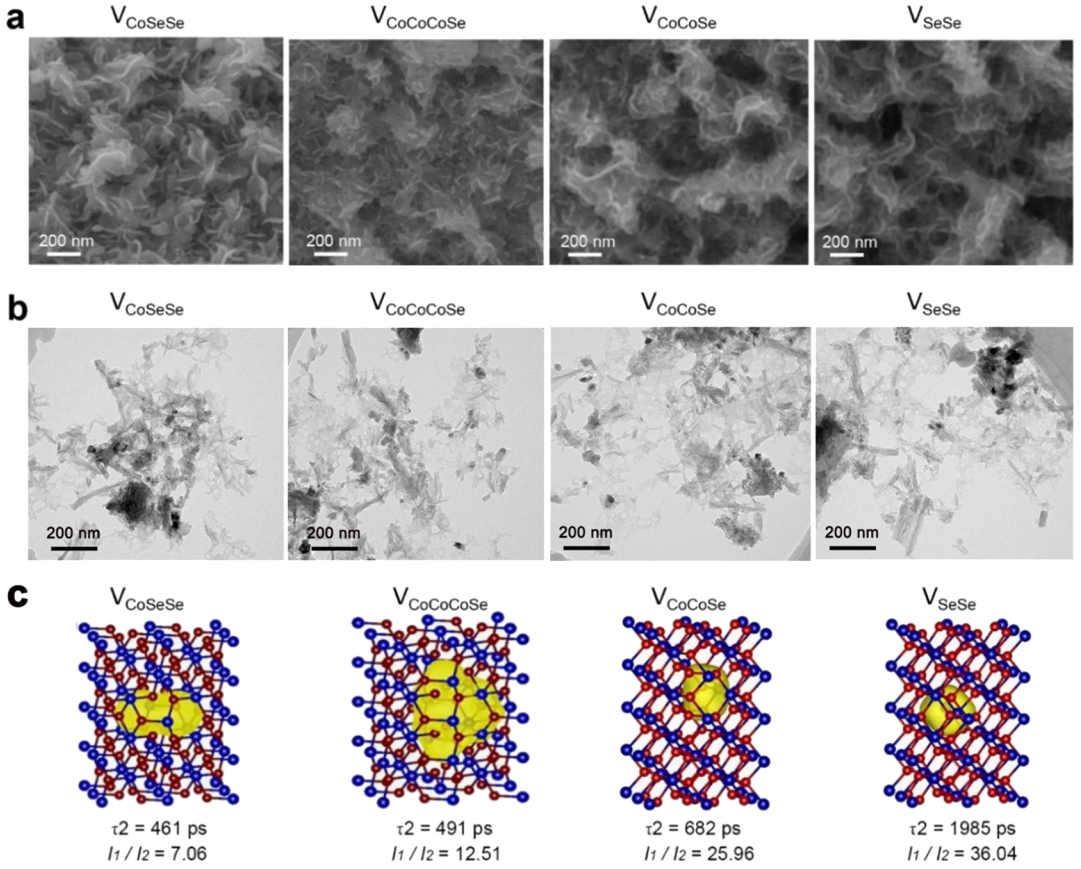


**Figure 2.** Morphology and vacancy type of the $CoSe_2$ nanosheets. (a) SEM images of the $CoSe_2$ nanosheets $V_{CoSeSe}$, $V_{CoCoCoSe}$, $V_{CoCoSe}$, and $V_{SeSe}$. (b) TEM images of the nanosheets. (c) Vacancy associates of the $CoSe_2$ nanosheets revealed by the positron annihilation spectra, showing increased $\tau_2$ from $V_{CoSeSe}$ to $V_{SeSe}$.

USA). To assess the toxicity of $CoSe_2$ nanosheets during coincubation of the tumor cells with the normal cells, the HeLa cells (tumor cells) transfected with the plasmid pEGFP-N1 (Clontech) (HeLa-GFP) were mixed with NIH3T3 cells (normal cells) with equal numbers in FBS-containing DMEM medium. The mixed cells were cultured for 24 h, and then the $CoSe_2$ nanosheets (20 mg/L) were added into the cell cultures. The cells were further cultured for 24 h, stained by propidium iodide (PI, 10 mg/L), and then examined by flow cytometry to count the PI-positive and GFP-positive cells (damaged tumor cells) and the PI-positive and GFP-negative cells (damaged normal cells).

**2.7. Flow Cytometry.** To assess the targeting specificity of $CoSe_2$ nanosheets, the HeLa-GFP cells were coincubated with NIH3T3 cells for 24 h, and then the rhodamine B-tagged $CoSe_2$ nanosheets (20 mg/L) were added to the cell cultures. The cells were further cultured for 24 h, washed with PBS, and examined by flow cytometry (FACSCalibur, Becton Dickinson, USA). Rhodamine B-positive and GFP-positive cells (*i.e.*, tumor cells targeted by $CoSe_2$ nanosheets) and rhodamine B-positive and GFP-negative cells (*i.e.*, normal cells targeted by $CoSe_2$ nanosheets) were recorded.

**2.8. LMP Assay.** Lysosomal membrane permeability (LMP) was detected by LysoTracker Red staining. Briefly, the nanosheet-treated HeLa cells on the well bottoms were immersed in 500 $\mu$L of PBS and stained with 5 $\mu$L of LysoTracker Red (10 $\mu$M, Beyotime, China) at 37 °C for 40 min. The cells were washed with PBS and observed using a fluorescence microscope (CKX41, Olympus, Japan). At least 20 fields were observed. Both the cells with whole cell distribution of fluorescence (LMP-positive) and total cells in each field were counted, and the percentage of LMP-positive cells was calculated.

**2.9. Adsorption Experiments.** Adsorption of the membrane phospholipid phosphatidylethanolamine (PE, SbaseBio, China) to both NPs was carried out in 40 mL vials. The vials contained 200 $\mu$L of 10 mg/mL nanosheet stock suspension (in 1:1 chloroform/methanol) and 10 mg/mL PE stock solution (in 1:1 chloroform/methanol), and the final liquid volume was adjusted to 10 mL with 1:1 chloroform/methanol, which is an amphibious solution mimicking the membrane.[44,45] The vials were shaken at 180 rpm and 37 °C for 24 h and the supernatant in each vial was used for determination of PE contents using the LC−MS system (LCMS-2020, Shimadzu, Japan). The percent of adsorbed PE was then calculated.

**2.10. TEM Observation of Tumor Cells.** To observe damage of the tumor cell membrane caused by the nanosheets, the treated HeLa cells were fixed by 2.5% glutaraldehyde for 24 h. The cells were then postfixed by 1% osmium tetroxide solution, dried, and observed by a transmission electron microscope (Tecnai G2 F-20, FEI, USA).

**2.11. *In Vivo* Tumor Model.** The animal experiments were approved by the Nankai Ethical Committee in compliance with the Chinese law on experimental animals. Female BALB/c mice were obtained from Beijing HFK Bioscience Company. The mice were raised with free access to food and water. Each group contained five mice. The mouse sarcoma S180 cells (Cell Resource Center, Chinese Academy of Medical Science, Beijing, China) were suspended in saline at a concentration of $10^7$ cells/mL, and 100 $\mu$L of the suspension solution was subcutaneously injected into the mice. After 7 days of inoculation, the Tf-coated nanosheets at 20 mg/kg (which did not exert detectable detrimental side defects at this dose) were injected into the tumor area. The common chemotherapeutic drug oxaliplatin at 5 mg/kg (no obvious toxicity) was also injected into the tumor areas as the positive control. The mice were fed for 12 additional days and then sacrificed using isoflurane. All efforts were made to minimize suffering. The tumors were sampled, photographed, and weighed. The sampled tumors were further fixed by 4% formaldehyde, embedded with paraffin, and sectioned into slices. The slices were stained by the hematoxylin and eosin staining kit


https://dx.doi.org/10.1021/acsabm.0c00981
ACS Appl. Bio Mater. 2020, 3, 7800−7809

(Beyotime, China) and observed by a light microscope (DM3000, Leica, Germany). In addition, the tumors were ground, and the tumor cells were obtained for the TdT-mediated dUTP nick-end labeling (TUNEL) assay and caspase-3 activity assay using corresponding assay kits (Beyotime, China).

**2.12. Statistical Analysis.** Each experiment was performed in triplicate under each tested condition, and reported values represent the mean ± standard deviation. Significant difference ($p < 0.05$) between the treatments was determined using Student's $t$ test or one-way ANOVA. All statistical analyses were performed using Statistical Packages for the Social Sciences (version 20.0).

## 3. RESULTS AND DISCUSSION

**3.1. Synthesis of $CoSe_2$ Nanosheets with Different Vacancies Can Be Controlled by the Choice of Template and Temperature.** Four kinds of $CoSe_2$ nanosheets were synthesized with similar morphological and chemical properties except for vacancy characteristics. These four nanosheets were prepared using the template TETA at 200 °C ($V_{CoSeSe}$) or 250 °C ($V_{CoCoCoSe}$) or using the template TEPA at 260 °C ($V_{CoCoSe}$) or 225 °C ($V_{SeSe}$). Scanning electron microscopy (SEM) and transmission electron microscopy (TEM) show that the four kinds of $CoSe_2$ exhibit nanosheet shapes with a thickness of 10−20 nm (Figure 2a,b). X-ray diffraction (XRD) patterns revealed that the precursor contributes to amorphous products (Figure S1). These nanosheets possess orthorhombic structures with lattice parameters of $a$ = 0.485 nm, $b$ = 0.583 nm, and $c$ = 0.363 nm (JCPDS no. 53-0449). Amplified TEM images confirmed that the nanosheets are typical nanosheets with lattice fringes of 0.29 nm (Figure S2).

Positron annihilation spectra revealed that the four kinds of $CoSe_2$ nanosheets yielded two lifetime components with corresponding relative intensities $I_1$ and $I_2$, as shown in Table 1, Table S1, and Figure 2c. The vacancy types of the nanosheets were confirmed by different positron lifetime $\tau_2$, *i.e.*, 461 ps ($V_{CoSeSe}$), 491 ps ($V_{CoCoCoSe}$), 682 ps ($V_{CoCoSe}$), and 1985 ps ($V_{SeSe}$),[46−48] and by the increased values of $I_1/I_2$, *i.e.*, 7.06 ($V_{CoSeSe}$), 12.51 ($V_{CoCoCoSe}$), 25.96 ($V_{CoCoSe}$), and 36.04 ($V_{SeSe}$).[49,50] Overall, the positron annihilation spectra confirmed that the $CoSe_2$ nanosheets prepared with different templates and calcined at different temperatures had distinctly different surface vacancy properties, while they shared similar morphological and chemical properties. As discussed below, these differences in surface vacancies had a significant impact on their biological effect during interaction with tumor cells.

**Table 1. Positron Lifetime Parameters of $CoSe_2$ Nanosheets with Different Vacancies**

| vacancy | $\tau_1$ (ps) | $\tau_2$ (ps) | $I_1$ (%) | $I_2$ (%) | $I_1/I_2$ |
|---|---|---|---|---|---|
| $V_{CoSeSe}$ | 338.1 | 461.0 | 87.6 | 12.4 | 7.06 |
| $V_{CoCoCoSe}$ | 322.7 | 491.0 | 92.6 | 7.4 | 12.51 |
| $V_{CoCoSe}$ | 358.7 | 682.0 | 96.3 | 3.71 | 25.96 |
| $V_{SeSe}$ | 346.6 | 1985.0 | 97.3 | 2.7 | 36.04 |

**3.2. Nanosheets with Different Vacancies Had Distinct Phospholipid-Binding and PM-Damaging Ability.** The PM is the first structure that exogenous NMs encounter when interacting with mammalian cells, and the PM phospholipids are the critical biomolecules in such interactions.[51] First-principles computations were performed using the PAW approach[40] to compare the adsorption energies between the nanosheets with different vacancies and PM phospholipids. These calculations show that the theoretical adsorption energies of $V_{CoSeSe}$, $V_{CoCoCoSe}$, $V_{CoCoSe}$, and $V_{SeSe}$ for phospholipid were (in increasing order) −0.05, −0.27, −0.36, and −0.71 eV/nm$^2$, respectively (Figure 3a,b).

We hypothesized that nanosheets with vacancies that result in higher phospholipid adsorption energies would have higher membrane-damaging capacity. To test this hypothesis, we measured the affinity of the nanosheets to the membrane phospholipid, PE.[52,53] Consistent with our hypothesis, (1) the adsorption affinity of PE to $CoSe_2$ nanosheets with different vacancies agreed with the theoretical adsorption energies (*i.e.*, $V_{SeSe} > V_{CoCoSe}$ $V_{CoCoCoSe} > V_{CoSeSe}$) (Figure 3c), and (2) the higher energy of adsorption correlated with damage to liposome membranes, as indicated by the release of the entrapped dye 5(6)-carboxyfluorescein, which leads to a significant increase in fluorescence intensity (Figure 3d). Clearly, nanosheets with different vacancies had different adsorption affinity to PE, which may result in different biological effects. Apparently, 2D NMs may penetrate the PMs with their sharp edges and extract the membrane phospholipids from the membranes, thus disrupting membrane integrity.[54,55] Overall, these results suggest that vacancy manipulation could regulate the phospholipid-binding and consequent membrane-disrupting ability of the nanosheets.

**3.3. Vacancy Types Strongly Affect Their Efficiency to Kill Tumor Cells.** Since the nanosheets with different vacancies had distinct phospholipid-binding and PM-damaging ability, we examined the cytotoxicity of four nanosheets to tumor cells (the human cervical cancer cells HeLa and the human lung cancer cells A549). As expected, the viability of both types of cells decreased with increasing energy of phospholipid adsorption (*i.e.*, $V_{SeSe} > V_{CoCoSe} > V_{CoCoCoSe} > V_{CoSeSe}$) (Figure 4a,b) For example, at 20 mg/L, $V_{SeSe}$ caused a 75−85% decrease in viability in the tumor cells ($EC_{50}$ = 10.2 ± 1.7 mg/L for HeLa cells and 8.2 ± 1.5 mg/L for A549 cells) and led to 43−45% cell death for both cells (Figure 3c,d), while $V_{CoSeSe}$ only caused a 41−46% decrease ($EC_{50}$ = 29.4 ± 2.8 mg/L for HeLa cells and 37.6 ± 2.5 mg/L for A549 cells) (Figure 4a,b) and a 7−9% cell death (Figure 4c,d).

Consistently, plasma membrane damage (evaluated by PI staining assay) and LMP (evaluated by LysoTracker Red staining assay) corroborated that $V_{SeSe}$ exerted the greatest damage to the plasma membrane and the lysosome, while $V_{CoSeSe}$ caused the least damage (Figure 4c−f). This supports the notion that vacancy engineering could be used to regulate the phospholipid-binding affinity of some 2D nanomaterials and consequently cell targeting and biological effects. In fact, Xu et al. have recently reported that 2D transition-metal dichalcogenides with different surface vacancies exhibited different activity in inducing cellular ferroptosis.[56]

**3.4. Toxicity of $CoSe_2$ Nanosheets Is Not Associated with Ion Dissolution and Oxidative Stress.** In addition to membrane damage, both ion dissolution and oxidative stress are frequently involved in nanotoxicity. Thus, the toxicity mechanism of $CoSe_2$ nanosheets was further investigated. First, we measured the dissolution of both $Co^{2+}$ and $Se^{-}$ from the nanosheets when they were coincubated with the cell culture medium and considered the potential toxicity of dissolved $Co^{2+}$ and selenium to the tumor cells. While the nanosheets at 20 mg/L released 0.9 to 1.7 mg/L $Co^{2+}$ and 2.4 to 5.8 mg/L selenium (Figure S3a,b), the released $Co^{2+}$ and selenium did not cause remarkable decrease in cell viability (Figure S3c,d). Hence, dissolution of $Co^{2+}$ and selenium did not contribute to the toxicity of the nanosheets. Moreover, the cells treated by


https://dx.doi.org/10.1021/acsabm.0c00981
ACS Appl. Bio Mater. 2020, 3, 7800−7809

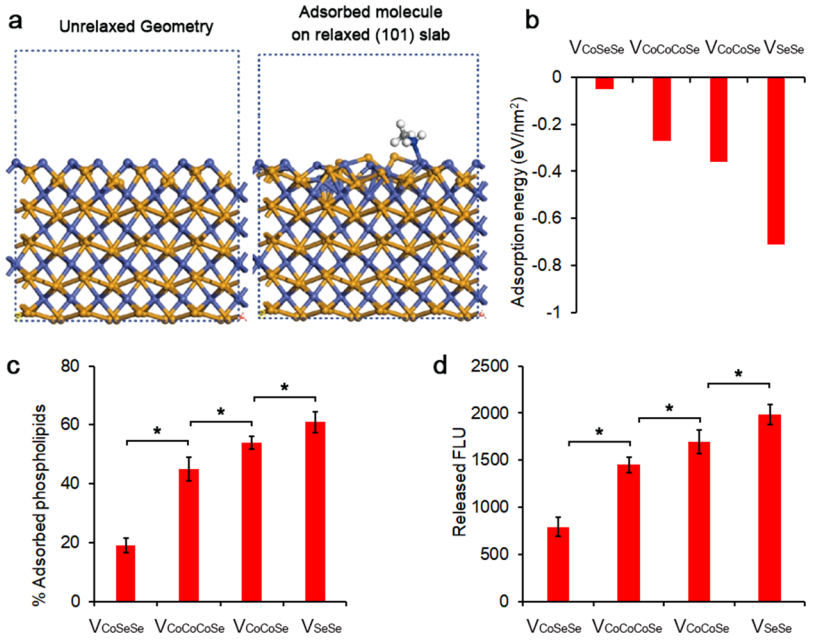


**Figure 3.** $CoSe_2$ nanosheets with different vacancies exhibit distinct interactions with the membrane phospholipids. (a) Geometric structures of the $CoSe_2$ (101) facets before relaxation and $CH_3NH_2$ molecule adsorbed on the fully relaxed $CoSe_2$ (101) slab. (b) Calculated adsorption energy of the nanosheets with $CH_3NH_2$, a model molecule of phospholipids. (c) Adsorption ability of the nanosheets with the phospholipid PE evaluated by adsorption experiment. (d) Damage of liposomes indicated by the released fluorescent dye 5(6)-carboxyfluorescein. Asterisks indicate significant difference between the groups ($p < 0.05$).

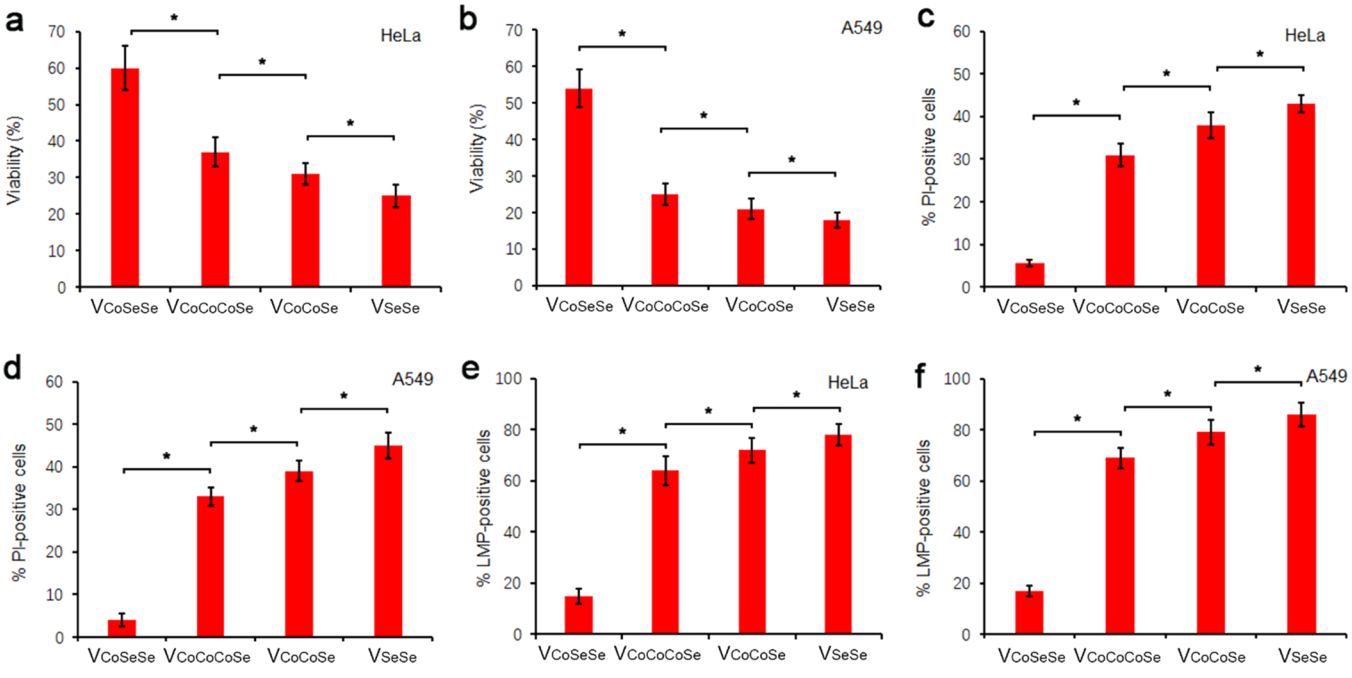


**Figure 4.** $CoSe_2$ nanosheets with different vacancies exhibit distinct toxicity to the tumor cells (a, c, e) HeLa and (b, d, f) A549. Panels (a) and (b) depict cell viability (the concentration of the nanosheets is 20 mg/L) evaluated by CCK-8 assay; panels (c) and (d) show death evaluated by PI staining and flow cytometry assay; panels (e) and (f) show LMP-positive cells evaluated by LysoTracker Red staining. Asterisks indicate significant difference between the groups ($p < 0.05$).

different nanosheets displayed similar reactive oxygen species (ROS) levels, and the ROS scavenger *N*-acetylcysteine could not rescue the viability of the treated cells (Figure S4). Thus, the different toxicity of the nanosheets is attributed to differences in their direct interaction with the cell membrane and resulting membrane damage rather than to ion dissolution and oxidative stress.

**3.5. Tf Coating Renders Specific Targeting and Efficient Killing of Tumor Cells.** To enhance specific targeting of tumor cells, the nanosheets with different vacancies were coated with Tf by binding of Tf thiol groups to active cobalt atoms on the surface of $CoSe_2$ nanosheets. Dynamic light scattering analysis revealed that the Tf coating onto the nanosheets led to a significant decrease in hydrodynamic sizes


https://dx.doi.org/10.1021/acsabm.0c00981
ACS Appl. Bio Mater. 2020, 3, 7800−7809

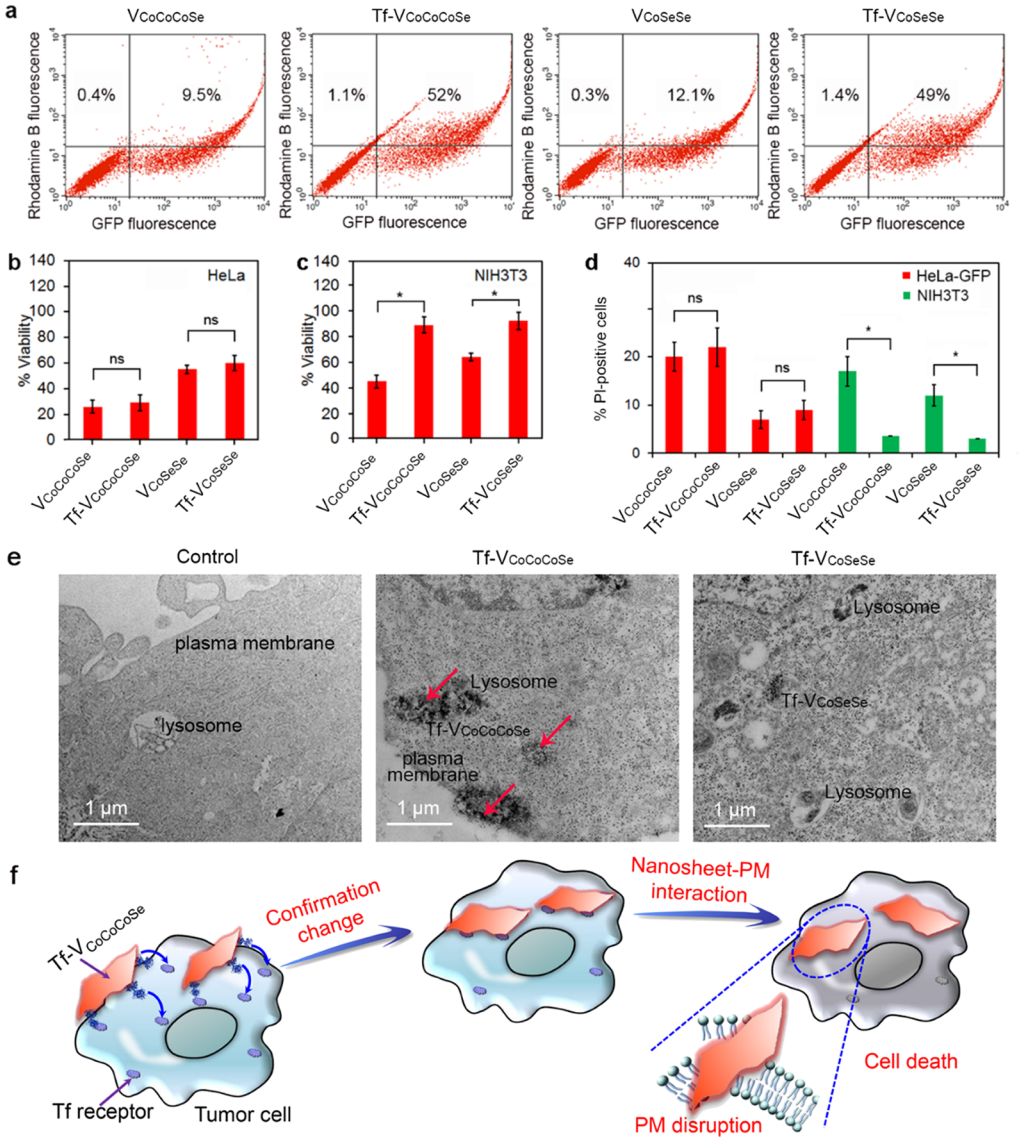


**Figure 5.** Tf coating to the $CoSe_2$ nanosheets facilitates specific targeting and damaging to tumor cells. (a) Rhodamine B-tagged and Tf-coated $CoSe_2$ nanosheets target the tumor cells (HeLa-GFP in the right quadrants) rather than normal cells (NIH3T3 in the left quadrants). FL1-H and FL2-H indicate the GFP fluorescence and the rhodamine B fluorescence, respectively. (b–d) Tf-coated $CoSe_2$ nanosheets (similar to the uncoated nanosheets) exhibit high toxicity to HeLa tumor cells (b, d) but had remarkable decreased toxicity to NIH3T3 normal cells (c, d). (e) TEM observation of the nanosheet-treated cells. The red arrows indicated the damaged membrane. Scale bars = 2 $\mu$m. (f) Suggested mechanisms of $CoSe_2$ nanosheet-caused cell death. The dark blue arrows indicate PM damage induced by the nanosheets. Asterisks indicate significant difference between Tf-$V_{CoCoCoSe}$ and Tf-$V_{CoSeSe}$ ($p < 0.05$), while "ns" indicates no significant difference.

of $V_{CoSeSe}$ and $V_{CoCoCoSe}$ from ~3000 to ~1139 nm but had no obvious impact on the sizes of $V_{CoCoSe}$ and $V_{SeSe}$ (Table S2). Since hydrophilic coatings of NMs may attenuate aggregation and consequently reduce hydrodynamic sizes, the drastic decrease in hydrodynamic sizes of $V_{CoSeSe}$ and $V_{CoCoCoSe}$ implies successful coating with Tf. In contrast, hydrodynamic sizes of $V_{CoCoSe}$ and $V_{SeSe}$ did not decrease significantly, indicating unsuccessful coating. The difficulty to coat $V_{CoCoSe}$ and $V_{SeSe}$ nanosheets with Tf might be due to the strong nanosheet–nanosheet interaction that hinders Tf binding to the nanosheets. FT-IR analysis further showed the presence of $-NH_2$ and $-CO-NH-$ on Tf-coated $V_{CoSeSe}$ and $V_{CoCoCoSe}$, confirming that Tf was coated onto both nanosheets (Figure S5). Moreover, while Tf-$V_{CoSeSe}$ and Tf-$V_{CoCoCoSe}$ did not impair the viability of normal cells, $V_{CoCoSe}$ and $V_{SeSe}$ after Tf coating still exerted some toxicity to the normal cells (Figure S6), which is a concern for *in vivo* applications. Therefore, we chose Tf-$V_{CoSeSe}$ and Tf-$V_{CoCoCoSe}$ for further anticancer investigations.

The specificity of both the bare and coated nanosheets toward tumor cells was examined using the tumor cell–normal cell coincubation system. As intended, Tf coating promoted the nanosheets to specifically target the tumor cells rather than the normal cells during coincubation of the green fluorescent protein (GFP)-tagged HeLa cells (HeLa-GFP, exhibiting strong green fluorescence) and the untagged NIH3T3 cells. For example, only 9.5% of the tumor cells (HeLa-GFP) or 0.4% of the normal cells (NIH3T3) were targeted by the rhodamine B-modified $V_{CoCoCoSe}$. In contrast, much more tumor cells were targeted by the Tf-$V_{CoCoCoSe}$ than the normal cells (52% versus 1.1%) (Figure 5a). Similar trends were observed for $V_{CoSeSe}$ (Figure 5a).


https://dx.doi.org/10.1021/acsabm.0c00981
ACS Appl. Bio Mater. 2020, 3, 7800–7809

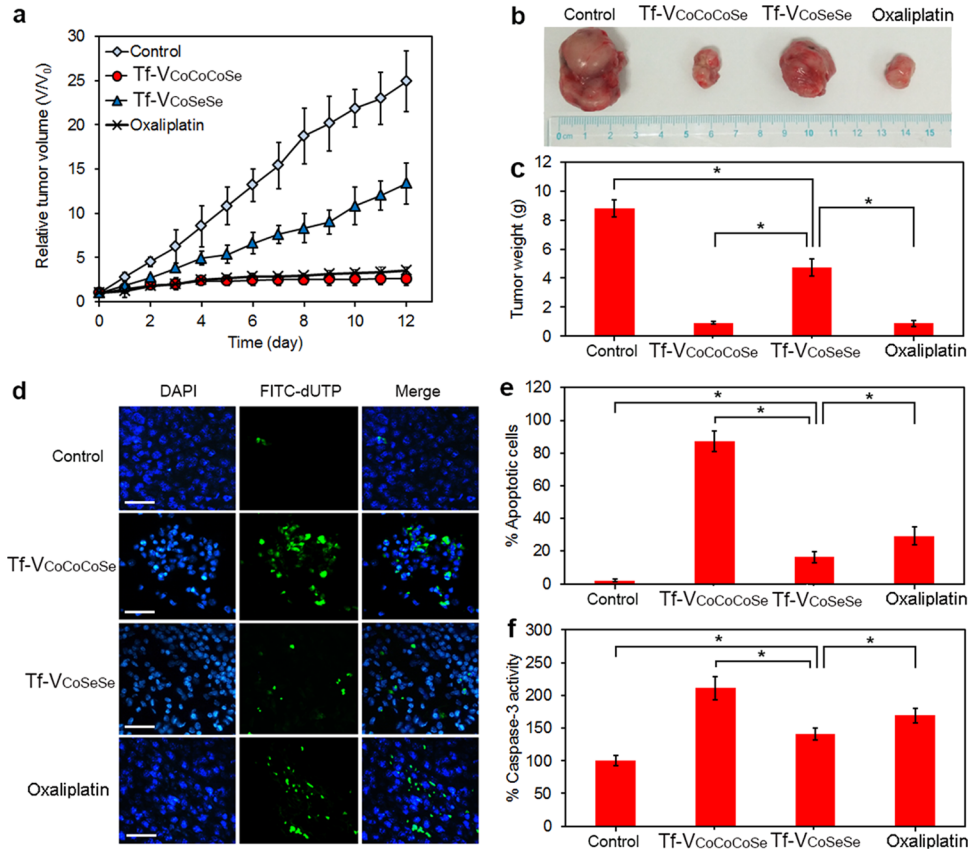


**Figure 6.** Tf-$V_{CoCoCoSe}$ exhibits much higher antitumor activity than Tf-$V_{CoSeSe}$. (a) Tumor growth inhibition profiles of the S180 tumor-burden mice after being intravenously injected with saline (control), suspensions of Tf-$V_{CoCoCoSe}$ or Tf-$V_{CoSeSe}$ (20 mg/kg), or oxaliplatin (5 mg/kg). (b) Photos of the tumors from the nanosheet-treated mice. (c) Tumor weights of different groups of the mice after 12 days of nanosheet treatment. (d) TUNEL assay of the tumor tissues sampled from the nanosheet- or oxaliplatin-treated mice. Scale bars, 20 $\mu$m. (e) Quantification of apoptotic (TUNEL-positive) cells. (f) Caspase-3 activity in the treated tumor tissues. Asterisks indicate significant difference between the treatments ($p < 0.05$).

Transferrin coating did not hinder the ability of the nanosheets to kill HeLa tumor cells, as indicated by the similar cytotoxicity of transferrin-coated $CoSe_2$ nanosheets (both Tf-$V_{CoCoCoSe}$ and Tf-$V_{CoSeSe}$) versus their corresponding uncoated controls (Figure 5b). Cells treated by the coated or uncoated $V_{CoCoCoSe}$ exhibited lower percentage of viability than those treated by $V_{CoSeSe}$ (26−29% versus 55−60%). However, for the normal cells (NIH3T3), Tf coating severely attenuated the affinity (and thus toxicity) of both nanosheets, with cell viability decreasing by less than 15% (Figure 5c). The specific toxicity of the coated nanosheets to tumor cells was confirmed by coincubation of HeLa-GFP with NIH3T3 cells. Similarly, Tf coating did not attenuate the toxicity of the nanosheets to the tumor cells but severely attenuated the toxicity to the normal cells (Figure 4d). Overall, Tf-$V_{CoCoCoSe}$ was more efficient for killing tumor cells than Tf-$V_{CoSeSe}$.

TEM analysis revealed that Tf-$V_{CoCoCoSe}$ caused more severe PM damage at nanosheet−PM contact sites than Tf-$V_{CoSeSe}$ and led to more severe lysosomal membrane damage by Tf-$V_{CoCoCoSe}$ than by Tf-$V_{CoSeSe}$ at the nanosheet−lysosomal membrane contact sites (Figure 5e). An increase in LMP results in the release of the acidic components and hydrolytic enzymes from the lysosome to the cytoplasm, which leads to cell damage.[57] The LMP assay also showed that $V_{CoCoCoSe}$ and Tf-$V_{CoCoCoSe}$ caused significantly more severe LMP than $V_{CoSeSe}$ and Tf-$V_{CoSeSe}$ (Figure S7a). Altogether, these observations indicate that $V_{CoCoCoSe}$ and Tf-$V_{CoCoCoSe}$ caused much higher membrane damage than $V_{CoSeSe}$ and Tf-$V_{CoSeSe}$, respectively. In addition, Tf coating led to a slight reduction in cytotoxicity of the nanosheets (Figure 5b−d), possibly due to the reduced contact between the nanosheets and the cell membrane.

Since $V_{CoCoCoSe}$ and Tf-$V_{CoCoCoSe}$ caused more severe damage to the PM and lysosomal membrane than $V_{CoSeSe}$ and Tf-$V_{CoSeSe}$, we hypothesized that these nanosheets had stronger interaction with the membrane components, which contributed to the higher cell death-inducing activity of $V_{CoCoCoSe}$ and Tf-$V_{CoCoCoSe}$ (Figure 5f). Similarly, both $V_{CoCoCoSe}$ and Tf-$V_{CoCoCoSe}$ had higher PE adsorption and liposome-damaging ability than $V_{CoSeSe}$ and Tf-$V_{CoSeSe}$ (Figure S7b,c).

**3.6. Tf-Modified $V_{CoCoCoSe}$ Nanosheets Strongly Inhibit Tumor Growth *In Vivo*.** Given that Tf-$V_{CoCoCoSe}$ specifically targeted and damaged the tumor cells *in vitro*, we proceeded to assess its efficacy for treating tumors *in vivo* using tumor-bearing mice. Compared with the untreated control group, Tf-$V_{CoCoCoSe}$-treated mice had substantially decreased tumor volumes (Figure 6a,b) and 9-fold reduction of tumor weight (Figure 6c). Most strikingly, the TUNEL assay further revealed that Tf-$V_{CoCoCoSe}$ killed a much higher percentage of cancer cells (~80%) than Tf-$V_{CoSeSe}$ (16%) and the common anticancer drug oxaliplatin (35%, applied at a typical dose of 5 mg/kg, since higher-level oxaliplatin has obvious toxicity to the mice, Figure S8 (Figure 6d,e). This result is consistent with the


https://dx.doi.org/10.1021/acsabm.0c00981
ACS Appl. Bio Mater. 2020, 3, 7800−7809

observation that Tf-$V_{CoCoCoSe}$ at 20 mg/L exhibited higher antitumor efficiency than oxaliplatin at the same concentration (Figure S9). The stronger antitumor efficiency of Tf-$V_{CoCoCoSe}$ nanosheets than oxaliplatin may be attributed to direct membrane damage and consequent cell death caused by the nanosheets rather than indirect DNA damage-induced cell death by oxaliplatin. The caspase activity assay also showed that the Tf-$V_{CoCoCoSe}$ nanosheets triggered much higher activity of caspase-3 (Figure 6f), an important factor inducing apoptosis. Hence, the Tf-$V_{CoCoCoSe}$ nanosheets showed strongest anticancer activity by severely killing tumor cells and disrupting tumor tissues. Importantly, the weights of the organs, including the liver, kidney, and spleen, remained stable under treatment with the nanosheets (Figure S10). Blood cell analysis showed that the TF-coated nanosheets did not cause obvious hemolysis (Figure S11). *In vivo* imaging further demonstrated that the nanosheets were located at the tumor region (Figure S12), confirming their targeting specificity to the tumor tissues. These observations suggest that Tf-$V_{CoCoCoSe}$ selectively targeted tumors and inhibited their growth without harming healthy organs.

## 4. CONCLUSIONS

Four types of $CoSe_2$ nanosheets with different vacancy associates (*i.e.*, $V_{CoSeSe}$, $V_{CoCoCoSe}$, $V_{CoCoSe}$, and $V_{SeSe}$) were synthesized by controlling templates and temperatures. The nanosheets with different vacancies exhibited different anticancer capacity due to their different affinity for cell membrane phospholipids and resulting ability to damage the lysosomes and plasma membranes. High selectivity toward cancer cells was achieved by successfully coating the $V_{CoSeSe}$ and $V_{CoCoCoSe}$ nanosheets with the tumor-targeting protein Tf. The Tf-coated $V_{CoCoCoSe}$ nanosheets (as compared to the Tf-coated $V_{CoSeSe}$) nearly fully eradicated mouse tumors in a short period of 12 days. The nanosheets did not exert noticeable detrimental side effects and outperformed the common chemotherapeutic drug oxaliplatin in eradicating malignant tumor tissues. These promising results suggest that controlled introduction of $CoSe_2$ nanosheet vacancies coupled with Tf coating could provide a novel and efficient route for cancer therapy that would circumvent drug resistance development.

## ■ ASSOCIATED CONTENT

### Supporting Information

The Supporting Information is available free of charge at https://pubs.acs.org/doi/10.1021/acsabm.0c00981.

Calculated positron lifetime values; hydrodynamic size distribution; XRD patterns; TEM images; $Co^{2+}$ and Se and oxidative stress contribution to the toxicity of nanosheets; FT-IR spectra; toxicity studies to tumor cells; impact of coated and uncoated nanosheets on LMP, phospholipid adsorption, and liposome damage; dose-dependent toxicity of oxaliplatin to mice; coated nanosheets impact on the weight of normal organs; coated nanosheets contribution to hemolysis; and nanosheets injected at the tumor site (PDF)

## ■ AUTHOR INFORMATION


### Corresponding Authors

**Qilin Yu** − *Key Laboratory of Molecular Microbiology and Technology, Ministry of Education, Department of Microbiology, College of Life Science, Nankai University, Tianjin 300071, P. R. China;* orcid.org/0000-0003-0473-5111; Email: yuqilin@mail.nankai.edu.cn

**Xiangsheng Liu** − *NanoSystems Institute, University of California, Los Angeles, California 90095, United States;* orcid.org/0000-0002-5719-2838; Email: xsliu@ucla.edu

**Pedro J. J. Alvarez** − *Department of Civil and Environmental Engineering, Rice University, Houston, Texas 77005, United States;* orcid.org/0000-0002-6725-7199; Email: alvarez@rice.edu

### Authors

**Mingyang Liu** − *Department of Civil and Environmental Engineering, Rice University, Houston, Texas 77005, United States*

**Wei Chen** − *Tianjin Key Laboratory of Environmental Remediation and Pollution Control, College of Environmental Science and Engineering, Nankai University, Tianjin 300350, China;* orcid.org/0000-0003-2106-4284

Complete contact information is available at: https://pubs.acs.org/10.1021/acsabm.0c00981


### Author Contributions

M.L. and Q.Y. synthesized and performed the chemical and biological experiments and material characterization. All authors analyzed and discussed the results. M.L., Q.Y., X.L., and P.J.J.A. wrote the main manuscript. W.C. and P.J.J.A. supervised the work and edited the final version after it was reviewed and agreed upon by all authors.

### Notes

The authors declare no competing financial interest.

## ■ ACKNOWLEDGMENTS

This work was supported by the Ministry of Science and Technology of China (grant 2014CB932001), the Tianjin Synthetic Biotechnology Innovation Capacity Improvement Project (TSBICIP-KJGG-006), the Natural Science Foundation of Tianjin (19JCZDJC33800), and the National Natural Science Foundation of China (grants 31870139, 21425729, and 21271108). Partial funding was provided by the NSF ERC for Nanotechnology-Enabled Water Treatment (EEC-1449500).

## ■ REFERENCES


(1) Chabner, B. A.; Roberts, T. G., Jr. Chemotherapy and the War on Cancer. *Nat. Rev. Cancer* **2005**, *5*, 65−72.

(2) Paz-Ares, L.; Luft, A.; Vicente, D.; Tafreshi, A.; Gümüş, M.; Mazières, J.; Hermes, B.; Çay Şenler, F.; Csőszi, T.; Fülöp, A.; Rodríguez-Cid, J.; Wilson, J.; Sugawara, S.; Kato, T.; Lee, K. Y.; Novello, S.; Halmos, B.; Li, X.; Kowalski, D. M. Pembrolizumab plus Chemotherapy for squamous Non−Small-Cell Lung Cancer. *New Engl. J Med.* **2018**, *379*, 2040−2051.

(3) Keklikoglou, I.; Cianciaruso, C.; Güç, E.; Squadrito, M. L.; Spring, L. M.; Tazzyman, S.; Cassará, A.; Guichard, M.; Iruela-Arispe, M. L.; Lewis, C. E.; Coussens, L. M.; Bardia, A.; Jain, R. K.; Pollard, J. W.; De Palma, M. Chemotherapy Elicits Pro-Metastatic Extracellular Vesicles in Breast Cancer Models. *Nat. Cell Biol.* **2019**, *21*, 190−202.

(4) Camidge, D. R.; Pao, W.; Sequist, L. V. Acquired Resistance to TKIs in Solid Tumours: Learning from Lung Cancer. *Nat. Rev. Clinic. Oncol.* **2014**, *11*, 473−481.

(5) Sui, X.; Chen, R.; Wang, Z.; Huang, Z.; Kong, N.; Zhang, M.; Han, W.; Lou, F.; Yang, J.; Zhang, Q.; Wang, X.; He, C.; Pan, H. Autophagy and Chemotherapy Resistance: A Promising Therapeutic Target for Cancer Treatment. *Cell Death Dis.* **2013**, *4*, e838−e838.

(6) Zhang, M.; Ma, Y.; Wang, Z.; Han, Z.; Gao, W.; Zhou, Q.; Gu, Y. A CD44-Targeting Programmable Drug Delivery System for Enhancing and Sensitizing Chemotherapy to Drug-Resistant Cancer. *ACS Appl. Mater. Interfaces* **2019**, *11*, 5851−5861.
(7) Malhi, S.; Gu, X. Nanocarrier-Mediated Drugs Targeting Cancer Stem Cells: An Emerging Delivery Approach. *Exp. Opin. Drug Deliver.* **2015**, *12*, 1177−1201.
(8) Wang, J.; Zhang, Y.; Jin, N.; Mao, C.; Yang, M. Protein-Induced Gold Nanoparticle Assembly for Improving the Photothermal Effect in Cancer Therapy. *ACS Appl. Mater. Interfaces* **2019**, *11*, 11136−11143.
(9) Peer, D.; Karp, J. M.; Hong, S.; Farokhzad, O. C.; Margalit, R.; Langer, R. Nanocarriers as an Emerging Platform for Cancer Therapy. *Nat. Nanotechnol.* **2007**, *2*, 751.
(10) Chiang, C.-S.; Lin, Y.-J.; Lee, R.; Lai, Y.-H.; Cheng, H.-W.; Hsieh, C.-H.; Shyu, W.-C.; Chen, S.-Y. Combination of Fucoidan-Based Magnetic Nanoparticles and Immunomodulators Enhances Tumour-Localized Immunotherapy. *Nat. Nanotechnol.* **2018**, *13*, 746−754.
(11) Yin, Q.; Shen, J.; Zhang, Z.; Yu, H.; Li, Y. Reversal of Multidrug Resistance by Stimuli-Responsive Drug Delivery Systems for Therapy of Tumor. *Adv. Drug Deliver. Rev.* **2013**, *65*, 1699−1715.
(12) Yu, Q.; Zhang, Y.-M.; Liu, Y. H.; Xu, X.; Liu, Y. Magnetism and Photo Dual-Controlled Supramolecular Assembly for Suppression of Tumor Invasion and Metastasis. *Sci. Adv.* **2018**, *4*, eaat2297.
(13) Huang, J.; Lin, C.; Fang, J.; Li, X.; Wang, J.; Deng, S.; Zhang, S.; Su, W.; Feng, X.; Chen, B.; Cheng, D.; Shuai, X. pH-Sensitive Nanocarrier-Mediated Codelivery of Simvastatin and Noggin Sirna for Synergistic Enhancement of Osteogenesis. *ACS Appl. Mater. Interfaces* **2018**, *10*, 28471−28482.
(14) Estanqueiro, M.; Amaral, M. H.; Conceiçao, J.; Lobo, J. M. S. Nanotechnological Carriers for Cancer Chemotherapy: the State of the Art. *Colloids Surf., B* **2015**, *126*, 631−648.
(15) Tong, L.; Zhao, Y.; Huff, T. B.; Hansen, M. N.; Wei, A.; Cheng, J. X. Gold Nanorods Mediate Tumor Cell Death by Compromising Membrane Integrity. *Adv. Mater.* **2007**, *19*, 3136−3141.
(16) Jain, P. K.; El-Sayed, I. H.; El-Sayed, M. A. Au Nanoparticles Target Cancer. *Nano Today* **2007**, *2*, 18−29.
(17) Tenorio-Pearl, J. O.; Herbschleb, E. D.; Fleming, S.; Creatore, C.; Oda, S.; Milne, W. I.; Chin, A. W. Observation and Coherent Control of Interface-Induced Electronic Resonances in A Field-Effect Transistor. *Nat. Mater.* **2017**, *16*, 208−213.
(18) Liu, Y.; Cheng, H.; Lyu, M.; Fan, S.; Liu, Q.; Zhang, W.; Zhi, Y.; Wang, C.; Xiao, C.; Wei, S.; Ye, B.; Xie, Y. Low Overpotential in Vacancy-Rich Ultrathin $CoSe_2$ Nanosheets for Water Oxidation. *J. Am. Chem. Soc.* **2014**, *136*, 15670−15675.
(19) Guan, S.; Wang, L.; Xu, S.-M.; Yang, D.; Waterhouse, G. I.; Qu, X.; Zhou, S. Vacancy-Enhanced Generation of Singlet Oxygen For Photodynamic Therapy. *Chem. Sci.* **2019**, *10*, 2336−2341.
(20) Li, W.; Niu, Y.; Wu, X.; Wu, F.; Li, T.; Hu, W. Heterostructured $CoSe_2$/$FeSe_2$ Nanoparticles with Abundant Vacancies and Strong Electronic Coupling Supported on Carbon Nanorods for Oxygen Evolution Electrocatalysis. *ACS Sustain.Chem. Eng.* **2020**, *8*, 4658−4666.
(21) Chhowalla, M.; Shin, H. S.; Eda, G.; Li, L. J.; Loh, K. P.; Zhang, H. The Chemistry of Two-Dimensional Layered Transition Metal Dichalcogenide Nanosheets. *Nat. Chem.* **2013**, *5*, 263.
(22) Tao, W.; Kong, N.; Ji, X.; Zhang, Y.; Sharma, A.; Ouyang, J.; Qi, B.; Wang, J.; Xie, N.; Kang, C.; Zhang, H.; Farokhzad, O. C.; Kim, J. S. Emerging Two-Dimensional Monoelemental Materials (Xenes) for Biomedical Applications. *Chem. Soc. Rev.* **2019**, *48*, 2891−2912.
(23) Tang, W.; Fan, W.; Zhang, W.; Yang, Z.; Li, L.; Wang, Z.; Chiang, Y.-L.; Liu, Y.; Deng, L.; He, L.; Shen, Z.; Jacobson, O.; Aronova, M. A.; Jin, A.; Xie, J.; Chen, X. Wet/sono-Chemical Synthesis of Enzymatic Two-Dimensional $MnO_2$ Nanosheets For Synergistic Catalysis-Enhanced Phototheranostics. *Adv. Mater.* **2019**, *31*, 1900401.
(24) Hu, T.; Mei, X.; Wang, Y.; Weng, X.; Liang, R.; Wei, M. Two-Dimensional Nanomaterials: Fascinating Materials in Biomedical Field. *Sci. Bull.* **2019**, *64*, 1707−1727.
(25) Chen, Y.; Tan, C.; Zhang, H.; Wang, L. Two-Dimensional Graphene Analogues for Biomedical Applications. *Chem. Soc. Rev.* **2015**, *44*, 2681−2701.
(26) Wang, Y.; Liu, X.; Zheng, C.; Li, Y.; Jia, S.; Li, Z.; Zhao, Y. Tailoring $TiO_2$ Nanotube-Interlaced Graphite Carbon Nitride Nanosheets for Improving Visible-Light-Driven Photocatalytic Performance. *Adv. Sci.* **2018**, *5*, 1700844.
(27) Zheng, H.; Ji, Z.; Roy, K. R.; Gao, M.; Pan, Y.; Cai, X.; Wang, L.; Li, W.; Chang, C. H.; Kaweeteerawat, C.; Chen, C.; Xia, T.; Zhao, T.; Li, R. Engineered Graphene Oxide Nanocomposite Capable of Preventing the Evolution of Antimicrobial Resistance. *ACS Nano* **2019**, *13*, 11488−11499.
(28) Nan, H.; Wang, Z.; Wang, W.; Liang, Z.; Lu, Y.; Chen, Q.; He, D.; Tan, P.; Miao, F.; Wang, X.; Wang, J.; Ni, Z. Strong Photoluminescence Enhancement of $MoS_2$ Through Defect Engineering and Oxygen Bonding. *ACS Nano* **2014**, *8*, 5738−5745.
(29) Lu, Y.; Jiang, Y.; Gao, X.; Wang, X.; Chen, W. Strongly Coupled Pd Nanotetrahedron/Tungsten Oxide Nanosheet Hybrids with Enhanced Catalytic Activity and Stability as Oxygen Reduction Electrocatalysts. *J. Am. Chem. Soc.* **2014**, *136*, 11687−11697.
(30) Yan, J.; Wang, T.; Wu, G.; Dai, W.; Guan, N.; Li, L.; Gong, J. Tungsten Oxide Single Crystal Nanosheets for Enhanced Multichannel Solar Light Harvesting. *Adv. Mater.* **2015**, *27*, 1580−1586.
(31) Huang, X.; Zhang, W.; Guan, G.; Song, G.; Zou, R.; Hu, J. Design and Functionalization of the NIR-Responsive Photothermal Semiconductor Nanomaterials For Cancer Theranostics. *Acc. Chem. Res.* **2017**, *50*, 2529−2538.
(32) Chen, T.; Li, S.; Wen, J.; Gui, P.; Fang, G. Metal−Organic Framework Template Derived Porous $CoSe_2$ Nanosheet Arrays for Energy Conversion and Storage. *ACS Appl. Mater. Interfaces* **2017**, *9*, 35927−35935.
(33) Fang, Y.; Yu, X.-Y.; Lou, X. W. D. Formation of Hierarchical Cu-Doped CoSe2 Microboxes via Sequential Ion Exchange for High-Performance Sodium-Ion Batteries. *Adv. Mater.* **2018**, *30*, 1706668.
(34) Zhang, K.; Park, M.; Zhou, L.; Lee, G. H.; Li, W.; Kang, Y. M.; Chen, J. Urchin-Like $CoSe_2$ as a High-Performance Anode Material for Sodium-Ion Batteries. *Adv. Func. Mater.* **2016**, *26*, 6728−6735.
(35) Sharma, S. K.; Pujari, P. K.; Sudarshan, K.; Dutta, D.; Mahapatra, M.; Godbole, S. V.; Jayakumar, O. D.; Tyagi, A. K. Positron Annihilation Studies in Zno Nanoparticles. *Solid State Commun.* **2009**, *149*, 550−554.
(36) Kuriplach, J.; Morales, A. L.; Dauwe, C.; Segers, D.; Šob, M. Vacancies and Vacancy-Oxygen Complexes in Silicon: Positron Annihilation with Core Electrons. *Phys. Rev. B* **1998**, *58*, 10475.
(37) Rauch, C.; Makkonen, I.; Tuomisto, F. Identifying vacancy Complexes in Compound Semiconductors with Positron Annihilation Spectroscopy: A Case Study of InN. *Phys. Rev. B* **2011**, *84*, 125201.
(38) Robles, J. M. C.; Ogando, E.; Plazaola, F. Positron Lifetime Calculation for the Elements of The Periodic Table. *J. Phys.: Condens. Matter* **2007**, *19*, 176222.
(39) Marrink, S. J.; Mark, A. E. Molecular Dynamics Simulation of the Formation, Structure, and Dynamics of Small Phospholipid Vesicles. *J. Am. Chem. Soc.* **2003**, *125*, 15233−15242.
(40) Kresse, G.; Joubert, D. From Ultrasoft Pseudopotentials to the Projector Augmented-Wave Method. *Phys. Rev. B* **1999**, *59*, 1758.
(41) Kresse, G.; Hafner, J. Ab Initio Molecular Dynamics for Liquid Metals. *Phys. Rev. B* **1993**, *47*, 558.
(42) Perdew, J. P.; Burke, K.; Ernzerhof, M. Generalized Gradient Approximation Made Simple. *Phys. Rev. Lett.* **1996**, *77*, 3865.
(43) Liu, L.; Zhang, L.; Wang, K.; Wu, H.; Mao, H.; Li, L.; Ding, S. Understanding the Dual-phase Synergy Mechanism in $Mn_2O_3$-$Mn_3O_4$ Catalyst for Efficient Li-$CO_2$ Batteries. *ACS Appl. Mater. Interfaces* **2020**, *12*, 33846−33854.
(44) Takai, Y.; Kishimoto, A. K. I. R. A.; Iwasa, Y.; Kawahara, Y.; Mori, T.; Nishizuka, Y. Calcium-dependent Activation of A


https://dx.doi.org/10.1021/acsabm.0c00981
*ACS Appl. Bio Mater.* 2020, 3, 7800−7809

Multifunctional Protein Kinase by Membrane Phospholipids. *J. Biol. Chem.* **1978**, *254*, 3692−3695.
(45) Yu, Q.; Wang, H.; Peng, Q.; Li, Y.; Liu, Z.; Li, M. Different Toxicity of Anatase and Rutile $Tio_2$ Nanoparticles on Macrophages: Involvement of Difference in Affinity to Proteins and Phospholipids. *J. Hazard. Mater.* **2017**, *335*, 125−134.
(46) Ogorodnikova, O. V.; Dubov, L. Y.; Stepanov, S. V.; Terentyev, D.; Funtikov, Y. V.; Shtotsky, Y. V.; Gutorov, K. Annealing of radiation-Induced Defects in Tungsten: Positron Annihilation Spectroscopy Study. *J. Nuc. Mater.* **2019**, *517*, 148−151.
(47) Hu, X.; Koyanagi, T.; Katoh, Y.; Wirth, B. D. Positron Annihilation Spectroscopy Investigation of Vacancy Defects in Neutron-Irradiated 3 C-SiC. *Phys. Rev. B* **2017**, *95*, 104103.
(48) Jiang, X.; Zhang, Y.; Jiang, J.; Rong, Y.; Wang, Y.; Wu, Y.; Pan, C. Characterization of Oxygen Vacancy Associates within Hydrogenated $TiO_2$: A Positron Annihilation Study. *J. Phys. Chem. C* **2012**, *116*, 22619−22624.
(49) Gao, M. R.; Yao, W. T.; Yao, H. B.; Yu, S. H. Synthesis of Unique Ultrathin Lamellar Mesostructured $Cose_2$−Amine (Protonated) Nanobelts in A Binary Solution. *J. Am. Chem. Soc.* **2009**, *131*, 7486−7487.
(50) Li, W.; Zamani, R.; Rivera Gil, P.; Pelaz, B.; Ibáñez, M.; Cadavid, D.; Cabot, A. CuTe Nanocrystals: Shape and Size Control, Plasmonic Properties, and Use as SERS Probes and Photothermal Agents. *J. Am. Chem. Soc.* **2013**, *135*, 7098−7101.
(51) Sohaebuddin, S. K.; Thevenot, P. T.; Baker, D.; Eaton, J. W.; Tang, L. Nanomaterial Cytotoxicity Is Composition, Size, and Cell Type Dependent. *Part. Fibre Toxicol.* **2010**, *7*, 22.
(52) Vance, J. E.; Tasseva, G. Formation and Function of Phosphatidylserine and Phosphatidylethanolamine in Mammalian Cells. *BBA-Mol. Cell Biol. Lipid.* **2013**, *1831*, 543−554.
(53) Dawaliby, R.; Trubbia, C.; Delporte, C.; Noyon, C.; Ruysschaert, J. M.; Van Antwerpen, P.; Govaerts, C. Phosphatidylethanolamine Is a Key Regulator of Membrane Fluidity in Eukaryotic Cells. *J. Biol. Chem.* **2016**, *291*, 3658−3667.
(54) Zou, X.; Zhang, L.; Wang, Z.; Luo, Y. Mechanisms of the Antimicrobial Activities of Graphene Materials. *J. Am. Chem. Soc.* **2016**, *138*, 2064−2077.
(55) Chen, J.; Zhou, G.; Chen, L.; Wang, Y.; Wang, X.; Zeng, S. Interaction of Graphene and Its Oxide with Lipid Membrane: A Molecular Dynamics Simulation Study. *J. Phys. Chem. C* **2016**, *120*, 6225−6231.
(56) Xu, S.; Zheng, H.; Ma, R.; Wu, D.; Pan, Y.; Yin, C.; Gao, M.; Wang, W.; Li, W.; Liu, S.; Chai, Z.; Li, R. Vacancies on 2D transition metal dichalcogenides elicit ferroptotic cell death. *Nat. Commun.* **2020**, *11*, 3484.
(57) Ferri, K. F.; Kroemer, G. Organelle-Specific Initiation of Cell Death Pathways. *Nat. Cell Biol.* **2011**, *3*, E255−E263.


https://dx.doi.org/10.1021/acsabm.0c00981
*ACS Appl. Bio Mater.* 2020, 3, 7800−7809